ACS APPLIED MATERIALS & INTERFACES

www.acsami.org

Research Article

Multifunctional Composite Binder for Thick High-Voltage Cathodes in Lithium-Ion Batteries

Lalith Rao, Xinwei Jiao, Chan-Yeop Yu, Adam Schmidt, Cody O'Meara, Jeremy Seidt, Jay R. Sayre, Yehia M. Khalifa, and Jung-Hyun Kim*

Cite This: *ACS Appl. Mater. Interfaces* 2022, 14, 861−872

Read Online

ACCESS | Metrics & More | Article Recommendations | Supporting Information

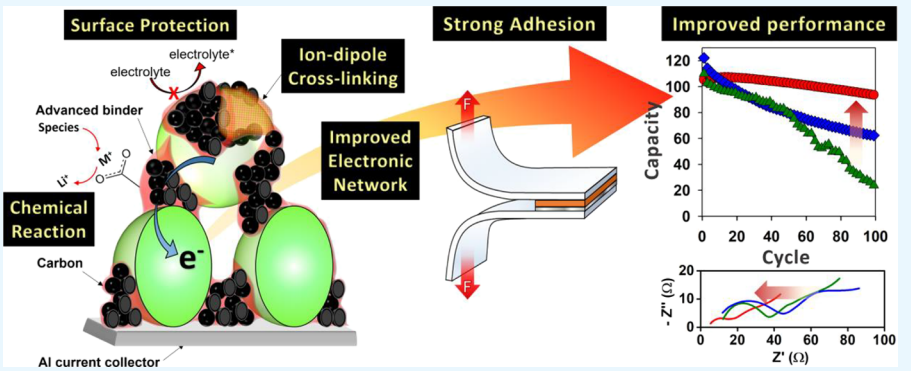

ABSTRACT: High-voltage $LiNi_{0.5}Mn_{1.5}O_4$ (LNMO) spinel offers high specific energy and good rate capability with relatively low raw-material cost due to cobalt-free and manganese-rich chemical compositions. Also, increasing mass loading (mg/cm^2) by thickening cathodes has been one of the focused areas to greatly improve the energy density of lithium-ion batteries (LIBs) at the cell level. The LNMO cathode made with a polyvinylidene fluoride (PVdF) binder, however, suffers from an oxidative decomposition of liquid electrolytes and cathode delamination from a current collector. This problem is exacerbated with an increase in thickness. In this study, we developed a lithium polyacrylate (LiPAA)−sodium alginate (Na-Alg) composite binder series that offer positive multifunctions such as enhancing cathode adhesion and cohesion, improving cycle life, creating an effective passivating layer at the cathode−electrolyte interface (CEI), and lowering cell impedance. Comprehensive design of systematic experiments revealed a close chemo-mechano-electrochemical relationship in the thick high-voltage cathodes. Among the various binder compositions, the LiPAA (30 wt %)−Na-Alg (70 wt %) binder offered a strong adhesion property and positive multifunctions at the CEI layer, which consequently stabilized the solid-electrolyte interfacial (SEI) layer on the graphite anode and improved LIB performances. This novel composite binder will be applicable to various types of thick cathodes in future studies.

KEYWORDS: *high-voltage $LiNi_{0.5}Mn_{1.5}O_4$ cathodes, thick cathodes, lithium polyacrylate and sodium alginate composite binders, adhesion force, full-cell performance*

INTRODUCTION

Ever since the commercialization of Li-ion batteries (LIBs) in 1991, energy storage technology has been revolutionized by allowing for portable devices, electronics, and now electric vehicles (EVs). High energy density and high power characteristics of LIBs, in addition to being sustainable for our future, make them attractive to find usage in various day-to-day applications.[1] Research in LIBs has focused toward improving the energy storage capability and reducing the costs.[2,3] To this end, promising approaches have been developed in terms of finding new cathode materials such as $LiNi_{1-x-y}Mn_xCo_yO_2$, $LiFePO_4$, $LiNi_{1-x-y}Co_xAl_yO_2$, and $LiNi_{0.5}Mn_{1.5}O_4$.

One of the most attractive approaches to improving LIB energy density is to increase the operating voltage.[4] In this regard, spinel-phase $LiNi_{0.5}Mn_{1.5}O_4$ (LNMO) is a promising cathode that has a high operating voltage (*ca.* 4.75 $V_{vs.\ Li}$) and reasonable discharge capacity (146.7 mAh g^{-1}).[5,6] Tetrahedral (8*a*) and octahedral interstitial (16*d*) sites provide three-dimensional Li^+ diffusion pathways through the spinel lattice, which offers excellent rate capability desired in automobile applications.[6] Furthermore, the low material cost of LNMO attributed to its cobalt-free and manganese-rich chemical

Received: October 10, 2021
Accepted: December 21, 2021
Published: December 29, 2021

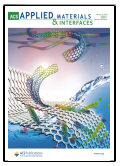

composition will be an enabler for a significant reduction of EV cost, considering that the cathode active material is responsible for around 45% of NMC/graphite cell cost.[7] For example, costs of cathode active materials are 47.51 USD kWh^{-1} for $LiNi_{0.6}Mn_{0.2}Co_{0.2}O_2$ (NMC622) and 21.09 USD kWh^{-1} for LNMO.[7] The cobalt-free LNMO will make LIBs independent to the ever-fluctuating cobalt price due to its global shortage.[7,8]

However, due to the high operating voltage of LNMO, oxidative decomposition of the electrolyte occurs at the cathode−electrolyte interface (CEI) in addition to other parasitic reactions, which lead to poor cycle life, especially at elevated temperatures.[9−11] The presence of carbon black and an unstable CEI has been shown to generate a lot of unwanted species such as PF_5, HF, and transition metal cations dissolved from LNMO, which lead to complex side reactions, consumption of active Li^+, and severe capacity fading.[12] Hence, there is a critical need to provide an effective passivating layer at the CEI, which can prevent such undesirable reactions. One promising approach has been using polymeric binders as coating agents.[12−14]

Traditionally, polyvinylidene fluoride (PVdF) has been used as a binder in cathodes due to its electrochemical stability and reasonable bonding strength.[15] However, it undergoes gelation and swelling in a liquid electrolyte, leading to reduced contact between particles especially after long-term cycling.[16] In particular, Lee et al.[17] reported a significant degradation of mechanical behaviors in a PVdF binder after immersing in an electrolyte by an operando AFM analysis. Moreover, PVdF does not offer protection against the parasitic reactions occurring at cathode−electrolyte interfaces at high voltages. This lack of passivation is due to the absence of active functional groups that can chemically interact with species present on particle surfaces.[12,18]

As an alternative, lithium polyacrylate (LiPAA) has been shown to provide positive multifunctions in high-voltage cathodes by (i) providing an effective passivating layer that stabilizes the CEI and (ii) donating extra Li^+ ions by absorbing protons, which significantly improved the long-term cycle life of LNMO/graphite full cells.[12] For example, the carboxylate functional group in LiPAA interacts with active oxygen atoms on LNMO surfaces and forms a conformal coating.[19] LiPAA is also an inexpensive water-soluble polymer with a very good binding property.[20] By replacing PVdF with LiPAA, one can benefit from eliminating the use of toxic NMP solvent (for PVdF) and making battery manufacturing environmentally friendly, along with reduction of processing and recovery costs of NMP.[2]

Despite all its desirable characteristics, we found that thick cathodes (e.g., >100 μm) made with a LiPAA binder are very brittle and prone to delamination upon bending. This makes it difficult to adopt in a roll-to-roll process and susceptible to mechanical degradation over continuous cycling. Hence, we developed composite binders having improved mechanical properties while retaining the important characteristics of LiPAA. Sodium alginate (Na-Alg) was chosen as the additive binder due to its good binding characteristics and demonstrated the capability to suppress capacity fading.[21] Na-Alg was first studied as a binder for Si anodes by Kovalenko et al.[22] It is derived from alginic acid, a family of natural copolymers of β-D-mannuronic acid (M unit) and α-L-guluronic acid (G unit).[23,23] Na-Alg is a water-soluble binder that forms a hydrogel due to the presence of hydroxyl and carboxylic groups.[24] Figure 1 illustrates the structure of Na-Alg in which a

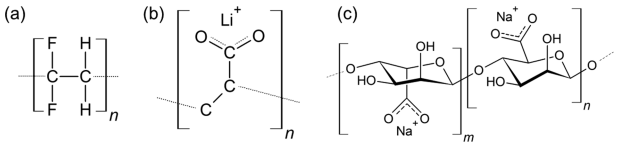

Figure 1. Molecular structures of (a) PVdF, (b) LiPAA, and (c) Na-Alg.

Na^+ ion is bonded to COO^- functional groups along the long chains of repeating alginate blocks. Better binding characteristics of Na-Alg over PVdF arise from these COO^- and OH^- functional groups in the long polymeric chains.[3] However, due to the absence of bivalent ions, Na-Alg does not exhibit crosslinking between two chains. Li^+ from LiPAA can attach itself to the COO^- groups in the M or G units of Na-Alg, which could potentially lead to the formation of crosslinking that would create a robust network, thereby enhancing the capacity.[25,26]

In this study, we investigated the effect of different combinations of LiPAA and Na-Alg binders on the mechanical and electrochemical properties of the electrodes. The amounts of LiPAA were varied from 100% to 0% while balancing the Na-Alg content to maintain the overall binder proportion in the electrode constant. The effect of binder compositions on the microstructure, adhesion force, binder properties, and electrochemical performances of LNMO cathodes will be presented.

EXPERIMENTAL SECTION

$LiNi_{0.5}Mn_{1.5}O_4$ (LNMO, MTI), PVdF (HSV 900), Super P carbon black (MTI), and Na-Alg (MP Biomedicals) were used as received. LiPAA solution (10 wt %) in water was prepared by mixing $LiOH·H_2O$ (Alfa Aesar), and 25 wt % of PAA solution (Sigma-Aldrich, $M_w \approx 240{,}000$) in water in a 1:1 molar ratio at pH 7. The amounts of LiPAA were varied from 100% to 0% while balancing the Na-Alg content to maintain the overall binder proportion in the electrode constant. Table 1 lists the nomenclature of LiPAA−Na-Alg composite binders used in this study with various compositions in the LNMO cathodes.

Table 1. Nomenclatures of LiPAA−Na-Alg Composite Binders with Various Compositions for LNMO Cathodes

sample	LiPAA (wt %)	Na-Alg (wt %)
LP100	100	0
LP70	70	30
LP60	60	40
LP50	50	50
LP40	40	60
LP30	30	70
LP0	0	100

The LNMO cathodes consisted of 85:7.5:7.5 wt % of LNMO:Super P:binder. Cathode slurries were prepared by adding 2.5 mL of solvent (e.g., NMP for the PVdF binder and water for LiPAA−Na-Alg binders) to 1 g of powders and mixing at 1000 rpm for 3 min (Thinky USA). The resulting slurry was then applied onto an aluminum foil current collector (MTI) using an automated film applicator and a doctor blade (thickness set to be 300 μm). The resulting cathode was dried at 80 °C for 30 min in a convection oven followed by vacuum drying at 120 °C overnight (12 h). The dried cathode was then roll-pressed at 80 °C through a calendering machine (MTI) targeting at ~40% porosity. Cathodes were then cut into circular discs (13.7 mm in diameter) using an electrode punch (Hohsen).

https://doi.org/10.1021/acsami.1c19554
ACS Appl. Mater. Interfaces 2022, 14, 861−872

The Al-clad coin cells (MTI, CR2032) were assembled in an argon-filled glovebox (LC Tech). The prepared circular disk of LNMO was used as the cathode, and lithium metal (0.75 mm in thickness, Alfa Aesar) for the half-cell was used as the anode. One hundred microliters of 1 M $LiPF_6$ in ethylene carbonate (EC)/ethyl methyl carbonate (EMC) with a 1:1 wt % ratio (Gotion) was used as the electrolyte with a piece of polypropylene separator (Celgard 2500). Coin cells were assembled and sealed using an electric crimper (MTI Corp.). Full coin cells were fabricated by pairing the cathodes with graphite anodes, which consists of an 89:1:3:7 wt % ratio of graphite:conductive graphite:Super P:PVdF. The N/P ratio was set to 1.05:1.

The morphological studies and elemental analysis of fresh and cycle-aged (after 100 cycles) LNMO cathodes were carried out by scanning electron microscopy (SEM, FEI Apreo LoVac) and energy-dispersive X-ray spectroscopy (EDS) at an operating voltage of 10 kV. A 180° peeling test of the cathodes was performed using a universal test machine with a load cell of 10 lbf. Sufficient time (10 min) was allowed for the adhesive tape to bond with both the electrode surfaces secured with jig clamps before testing. Three electrode samples with dimensions of 30 mm (L) × 13.5 mm (W) were measured at 0.025 in/s of peeling rate, and the average adhesion force was determined. The measured peel force was normalized with respect to the thickness of the electrode to ensure consistent comparison. The measured values for the peel force were obtained in mN mm^{-1}, which are used to compare to values reported in the literature. The normalization with respect to thickness has the units of mN mm^{-2}, and these values are used for the comparison between different binder compositions. After the full cells were discharged to 3.4 V after 100 cycles, the cells were disassembled in the glovebox. The cathode and anode from each of the cycled cells were washed separately with DMC for 5 min to remove electrolyte residues. After this, the samples were dried in an oven for 30 min and then used for further analysis. The attenuated total reflectance-Fourier transform infrared (ATR-FTIR; Reinshaw) spectra of pristine and cycled cathode surfaces were obtained with a spectral resolution of 8 cm^{-1} while purging N_2 gas. The acquired FTIR spectra were baseline-corrected and analyzed using OMNIC software. X-ray photoelectron spectroscopy (XPS, Kratos AXIS with a Mg Kα source) analysis was performed on fresh and cycled cathodes and anodes. To minimize surface charging, charge neutralization was enabled, and the spectra were calibrated based on C−C peaks at 284.7 eV. The resulting spectra were fit using the CasaXPS software package.

Electrochemical charge−discharge cycles of coin cells were performed in a potential range of 3.5−5 $V_{vs.\ Li}$ for half-cells and 3.4−4.9 V for full cells by using a multichannel battery testing station (Arbin Instruments) in an environmental chamber at 25 °C. Electrochemical impedance spectroscopy (EIS, Gamry Instruments) was performed for full cells during the third charge cycle at 4.7 V, which corresponds to approximately 50% of state of charge (SOC). The EIS characterization was performed by applying an alternating current of 50 μA in a frequency range of 100 kHz to 0.1 Hz. Before each EIS measurement, cells were rested for 30 min to reach their open-circuit voltages (OCVs).

RESULTS AND DISCUSSION

To investigate the effect of the binder on cathode performance, the following experimental parameters have been maintained throughout this study. The pH of LiPAA and Na-Alg was measured during each experiment to ensure its neutrality (i.e., pH value of ∼7.0). Solid loading of the cathode slurry was maintained at ∼33 wt %. The final thickness of the cathode was maintained to be ∼120 μm with ∼40% porosity after the calendering process.

Microstructure and Adhesion Property. The microstructure of the electrode is a critical parameter that governs the electrochemical performances of battery cells. The binder is the only component that offers adhesion or cohesion between active material, conducting agents (e.g., nano- and microsized carbons), and a current collector to build 3-D microstructures within electrodes. Therefore, we first observed the microstructures of uncalendered electrodes (i.e., as-prepared electrodes before their roll-pressing) with different composite binders by using SEM. Figure 2a,b respectively shows the comparison of the cathode microstructures between a baseline PVdF and LP30 (i.e., 30% LiPAA−70% Na-Alg) as a representative composite binder. The LNMO particles have polyhedron-shaped morphology with sizes of approximately 2−5 μm. In Figure 2a, the LNMO particles are clearly observable, while there is not much indication of carbon-binder distribution. The LNMO−binder/carbon distribution is clearly observable via backscattered electron (BSE) images from the cathodes as shown in Figures S1−S3. The large atomic-number disparity between LNMO and the carbon-binder composite leads to a large contrast in the BSE images. In particular, the BSE from the PVdF binder has a high tonal contrast, indicating a severe separation between white (from LNMO) and black (from carbon-binder) as shown in Figures S1a and S2. Lengths of the black-colored domains (i.e., carbon-binder) span from tens of micrometers to ∼100 μm. As a result, the carbon-binder distribution was not very homoge-

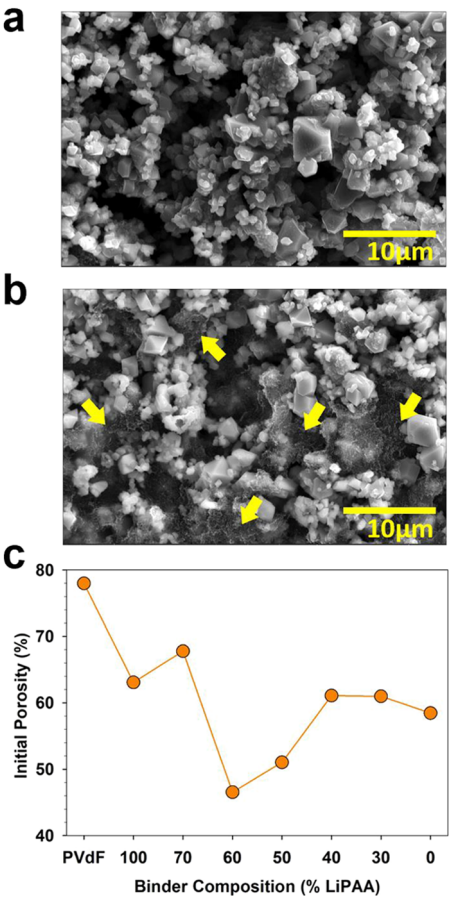

Figure 2. Representative SEM images of LNMO cathodes made with (a) a PVdF binder and (b) LP30 binder, which show binder coverage over LNMO particles (indicated by arrows). (c) Initial porosity of the LNMO cathodes from the different binder compositions. Both SEM images and initial porosity values were collected from uncalendered electrodes.

https://doi.org/10.1021/acsami.1c19554
ACS Appl. Mater. Interfaces 2022, 14, 861−872

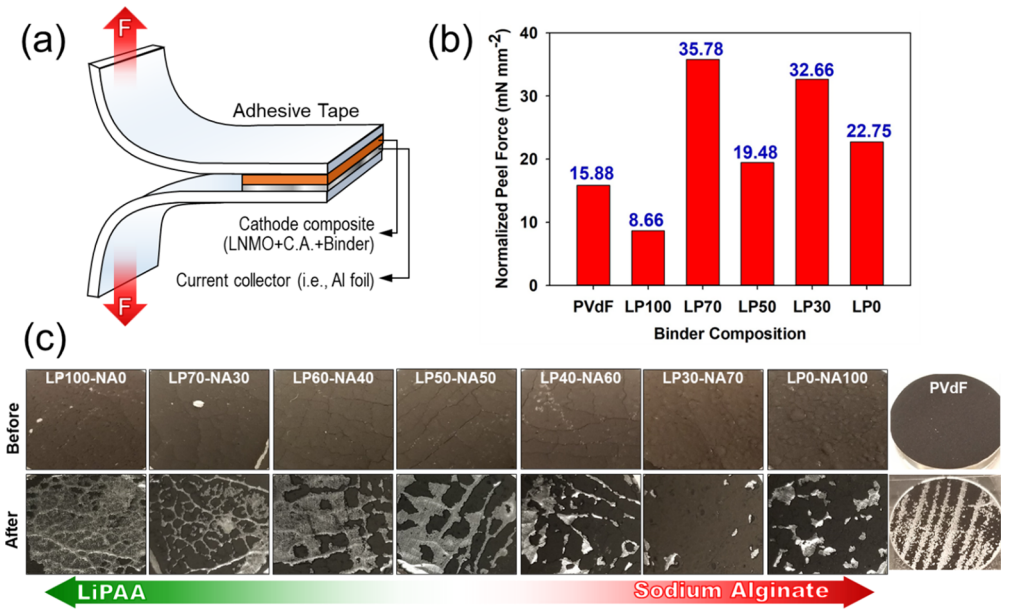

Figure 3. (a) Schematic illustration of the 180° peel test and (b) thickness-normalized peel force measurements for LNMO cathodes made with different binder compositions. (c) Images of LNMO cathodes before and after the peeling test.

neous in the LNMO-PVdF cathode as shown in Figure 2a and Figure S2.

In contrast, all the LP-series composite binders revealed a better distribution between LNMO and the carbon-binder as evidenced by a web-like layer (i.e., carbon-binder) over the LNMO particles, highlighted by arrows in Figure 2b. In addition, the BSE image of the LP100 cathode (see Figure S1b) has a much lower tonal contrast, indicating an improved carbon-binder distribution across the cathode. The light gray- and dark gray-colored domains respectively are associated with LNMO-rich and carbon-binder-rich regions. These microsized regions are different from the LNMO-PVdF microstructures in that they still maintain a good electrical contact via improved carbon-binder distribution across the thick cathodes. For example, Figure S3 reveals the presence of the good carbon-binder distributions when the cathodes were prepared with the LP-series binders. These results agree well with prior publication data for the LiPAA binder (LP100 in this work) and can be explained by the intrinsic uniformity of the LiPAA coating onto LNMO and the carbon conductor.[12]

It is important to emphasize that the binder should be able to homogeneously disperse and anchor carbon particles around the active materials for a good electrical contact. It was reported that either Na-Alg or LiPAA binders can deliver multiple advantages over the conventional PVdF binder in this perspective. While the PVdF binding relies on weak van der Waals interaction, functional groups in Na-Alg or LiPAA interact with hydroxyl species and/or active oxygen atoms on surfaces of LNMO and the carbon conductor via hydrogen bonding and/or covalent bonding, offering a much higher adhesion force.[12,17,27,28] In addition, Na-Alg or LiPAA has lower electrolyte uptake that positively retains mechanical properties (e.g., modulus and adhesion force) of binders after wetting them in liquid electrolytes.[3,17] Finally, these aqueous binders offer positive multifunctions such as the passivation of the electrode surface, proton scavenging, extra Li-ion source from LiPAA, and homogeneous distribution of carbons on LNMO surfaces from Na-Alg.[12,29]

Since the cathode compositions and processing conditions (e.g., solid loading of slurry and drying condition) remained constant, it would be reasonable to assume that the initial porosity value obtained from the uncalendered cathodes (i.e., as-prepared without roll-pressing) can be a good indicator for dispersion and loading of the electrode. The methods of determining the apparent density and porosity values, as well as the electrode mass loadings, are presented in the Supporting Information. Figure 2c shows that using the PVdF binder resulted in the highest porosity value (~79%) among the group; it also has the lowest areal loading among all the binder combinations tested. In contrast, uncalendered cathodes made with LP100 (i.e., pure LiPAA) and LP0 (i.e., pure Na-Alg) binders deliver lower porosity values and higher areal loadings. The porosity values show a trend of V-shaped valley with the minima from the LP60 binder (also having the highest areal loading). The lower initial porosity results from the contracting of slurry on the current collector surface in the case of LP-NA binders. From Figure 2a–c, it can be concluded that the electrodes resulting from LP-NA binders have more homogeneous and dense particle distribution.

Calendering is an important compaction process that affects mechanical properties and microstructures of electrodes and therefore impacts the battery performances. As noted earlier, all the LNMO cathodes prepared with various binders were calendered, targeting at ~120 μm thickness and ~40% porosity. Then, we characterized the effect of binder compositions on the adhesion forces of the calendered cathodes on the Al current collector. It was performed via a 180° peeling test as illustrated in Figure 3a. The force required to peel the electrode and current collector apart and the amount of material removal from the current collector can provide qualitative information about the adhesion strength.[30] Figure 3b compares the normalized peel forces of the LNMO cathode that significantly vary depending on binder compositions. As a baseline, the PVdF binder delivered a peel force of 22.68 mN mm^{-1} (before the conversion to mN mm^{-2}), which is close to a literature value of 24.85 mN mm^{-1}.[12] The LP100 cathodes delivered a peel force of 10.82 mN mm^{-1} (before the

https://doi.org/10.1021/acsami.1c19554
ACS Appl. Mater. Interfaces 2022, 14, 861–872

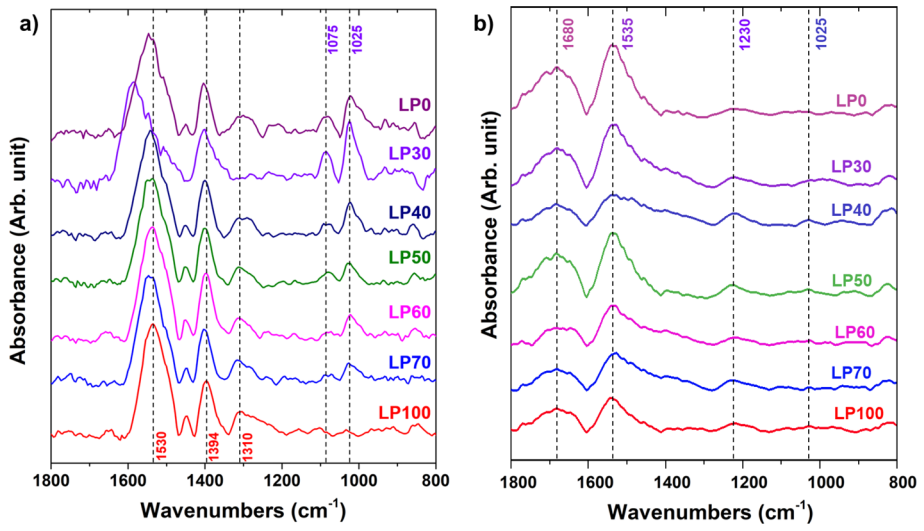

Figure 4. ATR-FTIR spectra obtained from the calendered LNMO cathode with different binder compositions (a) before cycling and (b) after 100 cycles.

conversion to mN mm^{-2}), which is much lower than a literature value of 37.61 mN mm^{-1} obtained from a thin electrode (i.e., less than 50 μm in thickness).[12] Since this work focuses on the thick cathode (e.g., ~120 μm in thickness), the low adhesion force of LP100 would be due to the severe crack generation (see Figure S1b) and possible delamination from the current collector, which is in part related to the brittleness of LP100.

Adding Na-Alg to the LiPAA binder significantly improved the adhesion properties of the LNMO cathodes. For example, LP70−LP0 cathodes delivered much higher adhesion forces than those of PVdF and LP100. It was reported that under neutral and mildly acidic conditions, the presence of hydroxyl (OH) groups increases the binding force to the Al current collector compared with that of carboxylic (COOH) groups,[31] which explains why LP0 having OH groups in Na-Alg shows better adhesion than LP100 having (COO^-) groups and PVdF having no functional group. When both hydroxyl and carboxyl functional groups exist together (i.e., LiPAA−Na-Alg composite), the ability to form complexes with the Al current collector can be improved due to ion−dipole interactions between functional groups of LiPAA and Na-Alg.[32] Therefore, the higher adhesion forces from the composite binders than end-members (LP100 and LP0) can be attributed to the optimized complexation from both functional groups.

After the top layer of the electrode was peeled off, the images of the residual current collector surface are shown in Figure 3c. First, it is notable that the strong interaction of electrodes during the drying process leaves unique wrinkles on the Al current collector in the case of the LiPAA−Na-Alg composite binders. When the electrode slurry is drying, the current collector is subjected to the stresses created by (i) the solvent being driven off a binder and/or (ii) chemical reaction of the binder (e.g., crosslinking of LiPAA) adhering onto the Al current collector. Second, when the adhesion between Al and the LNMO cathode layer is stronger than the adhesion between the tape and the cathode layer, there are residual materials remaining onto Al. For example, the PVdF electrode shows a pattern of lines of residual material and LP100 showed only a little to no residual electrode material, showing poor interfacial contact. With the introduction of Na-Alg, however, more electrode residual material was left on Al due to better binding characteristics.

FT-IR Analysis. ATR-FTIR spectroscopy was performed on the calendered cathodes to understand interactions between composite binders. Figure 4a shows the spectra obtained for the LNMO cathodes made with LP-series binders. The LP100 spectrum shows characteristic peaks at 1530 and 1394 cm^{-1} corresponding to the carboxylate group ($-COOLi^+$) and at 1446 cm^{-1} corresponding to C−H and CH_3 bending due to the carboxylate group.[12] The LP0 spectrum shows dominant peaks at 1542 and 1402 cm^{-1} but with smaller peak intensity, and the peak at 1446 cm^{-1} is suppressed due to lesser C−H bending. It is notable that two broad peaks at 1075 and 1025 cm^{-1} associated with the C−O stretching are absent from LP100. If there are no intermolecular interactions between LiPAA and Na-Alg, the spectra of the composite binders should be the representative of their individual spectra without any shifting or emergence/diminishing of peaks. However, that was not the case. In the case of the LP30 spectra, the carboxylate peaks shifted to 1585 cm^{-1} (from 1530 cm^{-1}) and 1403 cm^{-1} (from 1394 cm^{-1}), indicating the stretching of C═O in the carboxylate group due to an interaction with the alginate binder.[33] The absence of a peak between 1700 and 1720 cm^{-1}, which is generally attributed to the esterification by anhydride formation, suggests that the crosslinking occurs due to ion−dipole interactions between the functional groups of the two binders. Further, in going from LP100 to LP0, the addition of Na-Alg shows the peaks at 1025 and 1075 cm^{-1} becoming more prominent. As stated earlier, these peaks correspond to C−O bond stretching, which means that the hydroxyl groups of Na-Alg are interacting with the $-COOLi^+$ of LiPAA. This is also substantiated with the reduction of peak at 1310 cm^{-1} (C═O stretching) as the electron cloud density of $-COONa^+$ is shared with $-COOLi^+$.

Half- and Full-Cell Performances. The effect of the composite binders on the battery cell performances was evaluated by using coin half-cells. Figure 5a shows the representative voltage profiles of the LNMO cathodes with selected binders collected at 25 °C. All the rest of data can be found in Figure S7a. The high-voltage plateau (4.7 $V_{vs.\ Li}$) corresponds to the Ni^{+2}/Ni^{+4} redox reaction and the presence

https://doi.org/10.1021/acsami.1c19554
ACS Appl. Mater. Interfaces 2022, 14, 861−872

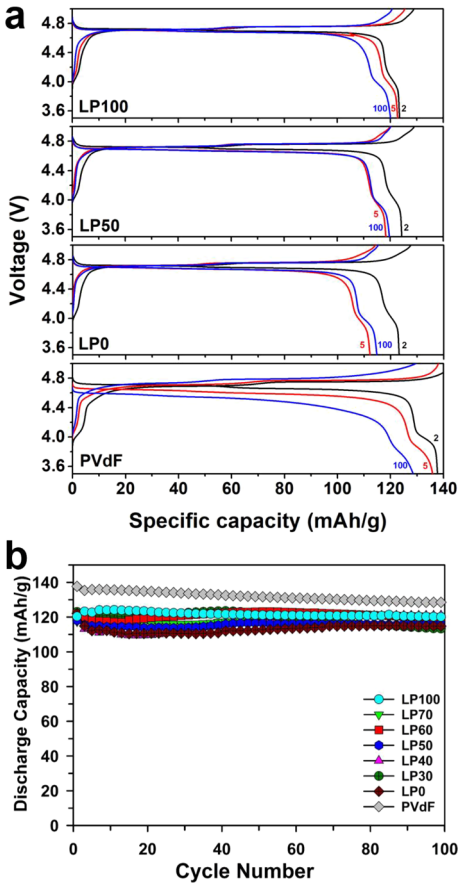

Figure 5. (a) Representative voltage profiles and (b) capacity retentions of LNMO/Li half-cells with different binders. All the cells were cycled at 0.1 C rate for initial two cycles and 0.2 C charge/0.5 C discharge for the rest at 25 °C.

of a small plateau at around 4 $V_{vs.\ Li}$ corresponds to the Mn^{+3}/Mn^{+4} redox couple.[34] Although LNMO with the PVdF binder delivers the highest initial discharge capacity (~139 mAh g^{-1}), it suffers from voltage drop during continuous cycling, indicating the unwanted increase in cell impedance during the cycling. This behavior agrees very well with literature data, which reported the formation of thick CEI and SEI layers on both LNMO and the Li metal and consequent impedance rise, which stem from parasitic reactions including the Mn dissolution from LNMO.[9,34,35] In stark contrast, all the LP-series binders offer stable operating potential of the cells during the 100 cycles, suggesting an effective suppression of parasitic reactions at the interfaces. dQ/dV profiles of the half-cells in Figure S7b show that average $Ni^{2+/4+}$ redox peak positions during charging vs discharging deviate by ~30 mV for LP-series cathodes and ~50 mV for the PVdF cathode, confirming the relatively large cell impedance from the PVdF cathode.

Half-cell cycle life in Figure 5b shows that the LP100 cathode exhibits a superior capacity retention of 97.4% after 100 cycles with an initial capacity of 125 mAh g^{-1} (0.5 C rate discharge capacity at the third cycle). The LP0 cathode (with pure Na-Alg binder) also delivers a good initial capacity of 123 mAh g^{-1}. The LP30−LP70 cathodes with the LiPAA−Na-Alg composite binders deliver similar initial capacity and cycle life during the 100 cycles in half-cells. All the LP-series cathodes using the LiPAA and/or Na-Alg binders showed capacity retentions superior to PVdF (93% at the 100th cycle) during 100 cycles. When the discharge rate was increased from 0.1 C to 0.5 C at the third cycle, the LP100 cathode showed negligible capacity drop compared to 8% capacity drop from the LP0 cathode (i.e., pure Na-Alg). This can be explained by the initial blocking of ion transfer via the Na-Alg polymer layer at the CEI. Due to volume changes occurring during repeated cycling, however, the polymer layer in LP0 may create channels for electrolyte penetration as evidenced by a gradual capacity increase from the 30th cycle.

It has been well understood that the major barrier of the high-voltage LNMO cathodes lies in a poor cycle life when paired with graphite anodes.[9,35] The performance degradation of the LNMO/graphite full cell is caused by a series of parasitic reaction mechanisms involving a production of side products at the CEI (e.g., HF and Mn^{2+}), their migration to the anode and attacking of the SEI layer on graphite, and regeneration of the SEI at the expense of Li ions and the electrolyte.[10] In the half-cell configuration, however, such capacity fading behavior cannot be observed because any Li loss will be compensated by a metallic Li anode. In this regard, we examined the full-cell performances of LNMO cathodes having various LiPAA−Na-Alg binder compositions.

Figure S8 shows the voltage profiles of the selected full cells at 2nd, 5th, and 100th cycles. Due to the Li^+ loss during the formation cycle of the graphite SEI, the PVdF cathode delivers a specific capacity of 122 mAh g^{-1} in the full cell, which is much lower (*ca.* 10% capacity loss) than its half-cell initial capacity of 135 mAh g^{-1}. In contrast, most of the LP-series cathodes deliver an initial discharge capacity of *ca.* ~115 mAh g^{-1} in full cells, which corresponds to ~4% capacity loss from its average half-cell capacity of ~120 mAh g^{-1}. This can be explained 2-fold: (i) extra Li^+ donation from LiPAA and/or (ii) passivation of the CEI that reduces parasitic reaction products and therefore suppresses extra Li^+ consumption during the graphite SEI formation.[12] In good agreement with literature data, Figure 6b shows a poor capacity retention of LNMO with a PVdF binder: 50.77% capacity retention at the 100th cycle at 25 °C.[12] Such capacity fading in the LNMO/graphite full cells is mainly caused by the loss of active Li^+ ions from LNMO due to the parasitic reactions.[9,10] Although the LP100 cathode has good initial performance (e.g., until 50 cycles), its capacity rapidly drops beyond 50 cycles due to the poor mechanical adhesion of the thick electrode (e.g., thickness of 120 μm) and consequent delamination of the cathode layer from the current collector. For example, well-established studies on thin LP100 and LP0 testing show that thin cathodes (e.g., less than 80 μm in thickness) consistently deliver good capacity retentions during the 100 cycles.[3,12] This result provides a rationale behind this work—the need to develop binder chemistry for thick high-voltage cathodes. At the same time, it should be noted that such cathode delamination has been reported to be a critical issue for the LNMO cathode with the PVdF binder during an extended period of cycling—even for the thin cathode.[12] Another end-member, the LP0 cathode with the pure Na-Alg binder, shows a good initial capacity of 114 mAh g^{-1} but also delivered a mediocre capacity retention of 68.4% at the 100th cycle.

It is important to note that the capacity retention data in Figure 6b clearly follow the same trend as the peel force data shown in Figure 3b. The LiPAA−Na-Alg composite binders (e.g., LP30, LP60, and LP70) can offer much improved capacity retentions of full cells compared with those from simple PVdF, LiPAA, and Na-Alg binders. In particular, the

https://doi.org/10.1021/acsami.1c19554
ACS Appl. Mater. Interfaces 2022, 14, 861−872

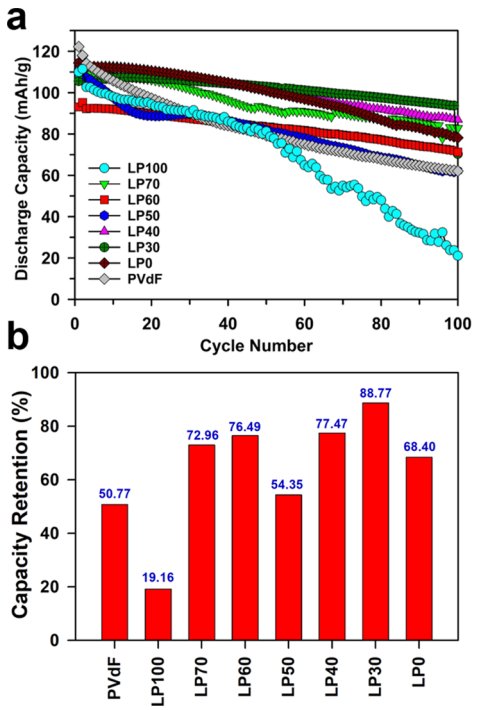

Figure 6. (a) Full-cell cycle life and (b) capacity retention percentiles (%) after 100 cycles. Initial two cycles at 0.1 C and remaining cycles at 0.2 C charge and 0.5 C discharge. Cycled at 25 °C between 3.4 V and 4.9 V.

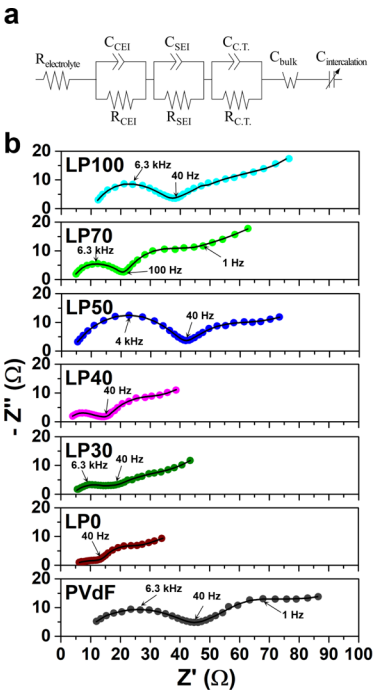

Figure 7. (a) Electrical circuit model (ECM) and (b) Nyquist plots of LNMO full cells measured at 4.7 V during the third cycle at 25 °C. Red dots are experimental data and solid lines are simulated data by the ECM.

LP30 cathode delivered 88.77% retention at the 100th cycle, which corresponds to 75% improvement compared with the conventional PVdF cathode. These results clearly demonstrate the importance of controlling mechanical properties of thick cathodes on the cycle life of full cells.

Electrochemical Impedance Spectroscopy (EIS) of Full Cells. EIS characterization was performed after charging the full cells to 4.7 V at the third cycle, followed by simulation using the equivalent circuit model (ECM) depicted in Figure 7a. Nyquist plots in Figure 7b contain a semicircle in a high-frequency region (*ca.* 100 kHz to 100 Hz), which can be associated with the combined CEI and SEI resistances ($R_{Interface}$).[34] The intercept of this semicircle at the *x*-axis is the uncompensated resistance (R_o), which includes the electrolyte resistance and any contact resistance. A semicircle at the medium-frequency region (*ca.* 100 Hz to 1 Hz) is attributed to charge transfer resistance, followed by Warburg-type solid diffusion in the active material particles at a low-frequency domain (*ca.* < 1 Hz). Compared to a half-cell where a more reactive Li metal causes a thicker SEI, the SEI layer on the graphite anode is smaller.[9] In Table 2, each Nyquist plot was simulated using the ECM and the sources of impedances were deconvoluted.

In the case of thin electrodes, provided that the cathode has a stable microstructure and good adhesion with a current collector, a major contributor to the high-frequency semicircle is the $R_{Interface}$ arising mainly from the CEI and SEI.[12,34] If the electrode has microstructural (e.g., crack) or composition issues (e.g., lack of binder contents in the electrode), however, the increase in the contact resistance at the cathode layer−Al current collector junction can become the dominant source of the high-frequency impedance.[3] Considering that electrolyte resistance and cell configuration remained the same for all full cells, the variations in R_o can originate from the poor contact within the cathodes. The high R_o values for the PVdF cathode (5.2 Ω) and LP100 cathode (10.52 Ω) well correspond to their low peeling forces shown in Figure 3b. On the contrary, LP70, LP30, and LP0 cathodes show nearly the same R_o values, which align very well with their good adhesion force. But LP50 has a higher value of R_o that can be associated with its low peeling force.

Table 2. Selected EIS Equivalent Circuit Model (ECM) Fitting Values

sample	R_o [Ω]	$R_{Interface}$ [Ω]
LP100	10.52	26.90
LP70	3.62	17.15
LP50	4.05	36.34
LP40	3.20	10.20
LP30	3.68	8.79
LP0	3.75	1.37
PVdF	5.20	32.82

The $R_{Interface}$ is associated with interfacial reactions such as binder surficial interaction with the electrolyte, Li-ion diffusion through CEI and SEI layers, and interaction of the carbon conductor with other components (e.g., active material and current collector).[3,34,36] It is difficult to deconvolute those impedance sources due to their time constants overlapping each other.[34] In our thick LNMO cathodes, the microstructure and adhesive/cohesive properties of cathode compositions can play a dominant role on the $R_{Interface}$ values in contrast to thin LNMO cathodes, which suffer less from microstructural defects and/or inhomogeneity. The $R_{Interface}$ values vary significantly depending on the binder compositions, which can be associated with the microstructures and/or mechanical property variations of the cathode, as shown in Figures 2 and 3.

https://doi.org/10.1021/acsami.1c19554
ACS Appl. Mater. Interfaces 2022, 14, 861−872

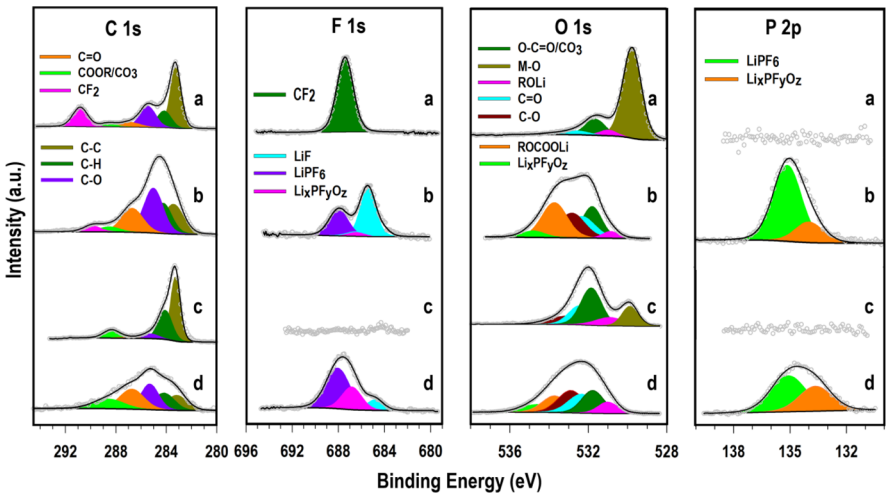

Figure 8. XPS C 1s, F 1s, O 1s, and P 2p spectra of (a) a fresh PVdF cathode, (b) 100 times cycled PVdF cathode, (c) fresh LP100 cathode, and (d) 100 times cycled LP30 cathode.

For example, Table 2 shows that the LP50 cathode, owing to its poor adhesion force, has a large $R_{Interface}$ value of ∼36 Ω, while the $R_{Interface}$ values decrease significantly from LP50 to LP0 cathodes, which aligned with their improved adhesion and capacity retention data. This result confirms the close relationship between adhesion, cycle life, and cell impedance in the thick high-voltage electrodes.

Characterization of Cycle-Aged LNMO Cathodes. The SEM images of the electrodes after 100 cycles as seen in Figure S4 show that for PVdF, LP0, and to a lesser extent in the LP100 electrode, the LNMO particles experienced degradation in the form of contours, spots, and etching on the surface. This is due to an insufficient passivation against electrolyte attack and also stresses generated during repeated electrochemical cycling. For the composite binder configuration, the LNMO particles retained most of their original surface and very less degradation of particles, indicating better passivation and robustness of the electrodes. Also, for the cycle-aged PVdF electrode, there appears to be more swelling, porosity, and less carbon-binder distribution compared to other compositions, which could lead to the loss of particle contact and consequent capacity fading.

To understand the elemental distribution in the electrodes, EDS analysis was performed on cathodes before and after cycling. Figure S5 shows the EDS maps of PVdF and the LP30 composite binder electrode. The EDS of pristine and cycled PVdF electrodes is consistent with what has been reported in the literature.[37] In the pristine PVdF electrode, neither carbon nor fluorine was detected. However, after 100 cycles, the amount of carbon and fluorine increased to 30.75 and 16.54%, respectively, while the Mn and Ni composition decreased as a fraction of the whole. The increase in C and F amount can be explained by a deposition of electrolyte decomposition products such as organic and inorganic forms of carbonates and LiF on the electrode surface.[35] In going from pristine to cycled PVdF, the decrease in detected O, Mn, and Ni amounts, which are from LNMO, is almost 50% for the same area analyzed (1 μm^2), which is indicative of a thick deposition layer over the cathode surface. In contrast, the cycled LP30 electrode still showed significant Ni, Mn, and O contents, suggesting that they have much less CEI layer on the particle surfaces. A small but noticeable distribution of phosphorus (P) was found from the cycled LP30 electrode, which was produced from the electrolyte decomposition. However, the amount of P was much lower (2.43%) than those of fluorine (16.54%) and carbon (30.75%) from the cycled PVdF electrode.

In Figure 4b, the ATR-FTIR spectra of the cycle-aged cathodes showed predominant peaks at 825, 1025, 1230, 1535, and 1680 cm^{-1}. While the peak at 1535 cm^{-1} is related to the carboxyl group in the binders, which is present in the pristine electrodes as well, other peaks are associated with the new CEI products on cathodes. The peak at 825 cm^{-1} corresponds to both C−H bending and C−C stretching. The peaks at 1025 and 1230 cm^{-1} are characteristics of strong C−O stretching, with the 1230 cm^{-1} peaks being more pronounced in the spectra. The peak at 1680 cm^{-1} indicates the strong stretching of C═O. These peaks are typical of poly(ethylene carbonate) (PEC) or poly(ethylene oxide) (PEO) species formed due to decomposition reactions in ethylene carbonate (EC)-based electrolytes.[38] The PF_5 anion acts as a catalyst for EC ring opening, leading to oxidative polymerization products such as PEC and PEO, as evidenced by the C═O stretching, followed by C−O/C−C stretching and C−H bending.[39]

To understand the surface chemistry and surface passivation offered by binders in forming the CEI and SEI, XPS characterization was performed. The CEI layers on cathodes and SEI layers on anodes continuously grow and evolve during the cycling.[40] In our study, the compositional variations of the CEI and SEI layers were due to the different types of binders we examined since the other testing conditions remained the same. The fresh LNMO-PVdF cathode, as shown in Figure 8a, has the major peaks including C−C (∼284.7 eV) from the carbon conductor, C−F (∼290.9 eV) and C−H (∼285.1 eV) from the PVdF binder,[41,42] and M−O (∼529 eV) peak from the metal (M)−O (∼529 eV) from LNMO. Since PVdF does not coat the surface of the LNMO cathode,[12] a strong M−O peak intensity can be observed. In contrast, the fresh LP100 cathode, as shown in Figure 8c, has reduced the intensity of the M−O peak in the O 1s spectrum, which can be explained by the surface coating of LiPAA on the LNMO particle.[12] The C−H peak, which is from the LiPAA binder, also has increased intensity, confirming that the binder is well dispersed on and around the surface of the electrode materials. From both PVdF

https://doi.org/10.1021/acsami.1c19554
ACS Appl. Mater. Interfaces 2022, 14, 861−872

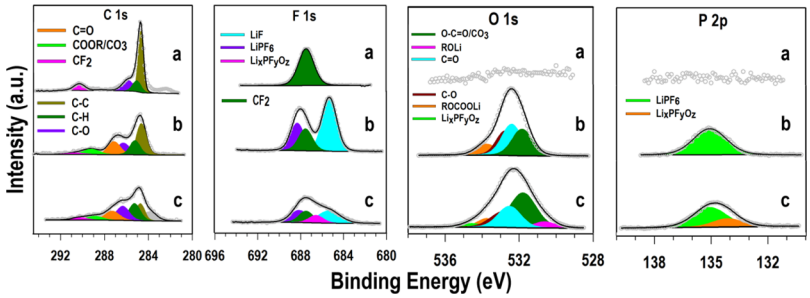

Figure 9. XPS C 1s, F 1s, O 1s, and P 2p spectra of (a) a fresh graphite anode, (b) 100 times cycled graphite anode paired with the PVdF cathode, and (c) 100 times cycled graphite anode paired with the LP30 cathode in full cells. All graphite anodes were made with the PVdF binder.

and LP100 cathodes, no peaks were observed from the P 2p spectrum since they were not cycled yet.

After 100 cycles, the LNMO-PVdF cathode had major C−O and C═O peaks from its C 1s and O 1s spectra. Also, the alkyl carbonate (ROCOOLi) in the O 1s spectra is the major product of EC decomposition.[43,44] This result agrees well with the ATR-FTIR data (see Figure 4b) and could be attributed to the production of the PEC-like phase.[39] In addition, LiF in the F 1s spectrum was the major product from the cycled LNMO-PVdF cathode. During cycling, $LiPF_6$ salt in the electrolyte decomposes into the intermediate product $Li_xPF_yO_z$ and finally to LiF.[45,46] The cycled LNMO-PVdF cathode had LiF as the major product while only having little amount of $Li_xPF_yO_z$, indicating that the decomposition reaction at the CEI progressed enough to reach the final stage. The $LiPF_6$ peak was from a trace amount of residual salt after washing the cathode using DMC solvent.

In comparison, the cycled LP30 cathode showed a much reduced LiF peak but had an increased $Li_xPF_yO_z$ peak in its F 1s spectrum (see Figure 8d), suggesting that the progress of parasitic reaction at the CEI was retarded. In addition, the intensities of C−O and ROCOOLi peaks in the O 1s spectra were lower than those of the cycled PVdF cathode, indicating that LP30 had less amount of decomposition products than the PVdF cathode.[47] Both PVdF and LP30 cycled cathodes did not show the M−O peak in the O 1s spectrum due to the production of the CEI layer on the electrode surface.

Characterization of Cycle-Aged Graphite Anodes. It has been well understood that the parasitic reactions occurring at the CEI result in the rapid degradation of the graphite SEI.[10] In particular, Mn dissolution from LNMO attacks the graphite SEI and leads to the unwanted Li-ion consumption during the recovery of the SEI.[9,35] Therefore, we performed EDS mapping of graphite anodes recovered from 100 times cycled full cells. The cycled graphite anode paired with the LNMO-PVdF cathode had 1.05% Mn from the impact of the Mn dissolution, as shown in Figure S6a. Also, it contained 29.4% F and 3.64% P, which are products of electrolyte decomposition in the SEI. In comparison, the cycled graphite anode paired with the LP30 cathode had 1.66% P but did not have Mn and F signals, suggesting that their amounts are smaller than detection limits. The result proves the effective CEI passivation function of the LP30 binder on LNMO cathodes.

Details of the chemical species on those cycled graphite anodes were characterized by XPS analysis. Figure 9 shows the XPS spectra of fresh and cycled anodes paired with PVdF and LP30 cathodes. The fresh graphite anode had CF_2 and C−H peaks in its F 1s and C 1s spectra since it was made with the PVdF binder. After cycling, the SEI consists of C−O, C═O, $LiPF_6$, $ROCO_2Li$, and LiF, which agrees well with the literature.[48] For the F 1s spectra, there are four main peaks, including $LiPF_6$, CF_2, $Li_xPF_yO_z$, and LiF. The high LiF content in the SEI film indicates higher consumption of lithium ions while also inhibiting the lithium diffusion due to its ionic conductivity that is at least three orders of magnitude lower than that in Li_2CO_3 and Li_2O.[49] Therefore, the low LiF intensity represents high conductivity and lower impedance of LNMO full cells. Among them, graphite paired with the LP30 cathode exhibited LiF peak intensity lower than that with the PVdF cathode in terms of both absolute intensity and relative intensity compared with the CF_2 peak from the PVdF binder. As observed from the cycled cathodes, the graphite SEI paired with the LP30 cathode had $Li_xPF_yO_z$ as the intermediate decomposition product, while the one paired with the PVdF cathode only had LiF without the $Li_xPF_yO_z$ product. This result suggests that the progress of parasitic reaction at the graphite SEI was retarded by employing the LP30 cathode, which agrees well with the XPS analysis on the cathode CEI.

CONCLUSIONS

Our study demonstrates clearly the positive multifunctions of the new LiPAA−Na-Alg (i.e., LP-series) composite binders in terms of the mechanical properties and electrochemical performances of the high-voltage LNMO cathodes. Despite many advantages of the LiPAA binder, it has difficulty in fabricating a thick electrode (e.g., >100 μm) due to its brittle properties arising during the drying process and consequent delamination issue. This issue can be resolved by adding Na-Alg, which has good elastic property, and overcoming the brittle nature of LiPAA.

The challenges toward achieving good performance in thick high-voltage cathodes are multifold including mechanical stability (i.e., delamination), inhomogeneous particle distributions, electrolyte decompositions at the CEI, transition metal dissolution, and subsequent loss of active Li at the graphite SEI. Our effort in this study is to emphasize the role of electrode properties (morphological, mechanical, and physicochemical) and how multifunctional composite binders can control these properties to mitigate the challenges and improve the cell performances. Figure 10 illustrates the positive multifunction of the LiPAA−Na-Alg composite binders in high-voltage cathodes. The SEM and EDS analyses confirmed that the composite binders offer better homogeneity and in turn provide an improved LNMO-C and C−C electronic network across the thick electrodes. In addition to their good individual adhesion properties, LiPAA and Na-Alg composite binders have the improved adhesion force in contact with the Al current collector at their optimal composition (e.g., LP30)

https://doi.org/10.1021/acsami.1c19554
ACS Appl. Mater. Interfaces 2022, 14, 861−872

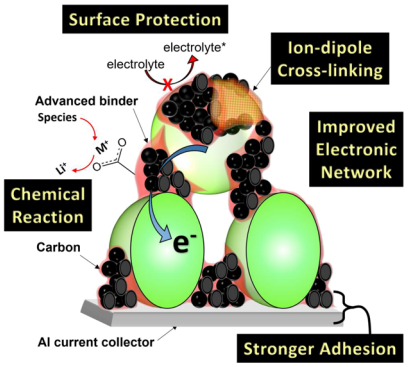

Figure 10. Schematic diagram illustrating positive multifunctions of LiPAA–Na-Alg composite binders in high-voltage LNMO spinel cathodes.

due to the ion–dipole interactions between their functional groups. These mechano-chemical properties strongly affected the LIB performances. For example, the trend in the adhesion (peel) force of cathodes was strongly correlated with their full-cell capacity retentions (see Figure 6) and EIS data (see Figure 7). For the latter, higher peel forces corresponded to lower R_o and $R_{Interface}$ values.

The LiPAA and Na-Alg composite binders also improved CEI stability as reported in the literature. The improvement mechanism has been known to be multifold including passivation of the electrode surface, proton scavenging, extra Li-ion source from LiPAA, and homogeneous distribution of carbons on LNMO surfaces from Na-Alg.[12,29] From these positive multifunctions, the LP30 cathode had a thinner CEI layer compared with the PVdF cathode after 100 times cycling (see Figure S5). In addition, low amounts of LiF and PEC-like phase in the LP30 cathode compared with that of the LNMO-PVdF cathode indicate that the LP30 binder lowers the rate of parasitic reactions at the CEI, as evidenced by ATR-FTIR and XPS analyses (see Figures 4b and 8). Such suppression of CEI reactions strongly affected the properties of the graphite SEI. The graphite cycled with the LP30 cathode had a minimal amount of Mn dissolution (below the detection limit of EDS) and a low amount of overall decomposition products including LiF compared to those from the PVdF cathode. As a result, the LP30 binder delivered the excellent adhesion forces and full-cell cycle life with low cell impedance; for example, it offered 75% improvement of full-cell life compared with the conventional LNMO cathode made with the PVdF binder. Even though an ~120 μm-thick high-voltage LNMO cathode was examined in this work, the LP-series composite binders would be useful in developing much thicker (e.g., >200 μm) cathodes in future studies.

■ ASSOCIATED CONTENT

Supporting Information

The Supporting Information is available free of charge at https://pubs.acs.org/doi/10.1021/acsami.1c19554.

Method of porosity calculation; backscattered electron (BSE) images of LNMO cathodes made with PVdF and LP100 binders; BSE images of fresh LNMO-PVdF cathodes; BSE images of fresh and cycle-aged LNMO cathodes made with various binder compositions; EDS data from LNMO-PVdF and LNMO-LP30 cathodes collected before and after cycling; EDS data from cycle-aged graphite anodes from full cells paired with LNMO-PVdF and LNMO-LP30 cathodes; voltage profiles and dQ/dV profiles of cathodes in half-cells with various binder compositions; voltage profiles of LNMO/graphite full cells with various binder compositions (PDF)

■ AUTHOR INFORMATION

Corresponding Author

Jung-Hyun Kim – *Center for Automotive Research, Department of Mechanical and Aerospace Engineering, The Ohio State University, Columbus, Ohio 43210, United States*; orcid.org/0000-0002-4598-4686; Email: kim.6776@osu.edu

Authors

Lalith Rao – *Center for Automotive Research, Department of Mechanical and Aerospace Engineering, The Ohio State University, Columbus, Ohio 43210, United States*

Xinwei Jiao – *Center for Automotive Research, Department of Mechanical and Aerospace Engineering, The Ohio State University, Columbus, Ohio 43210, United States*

Chan-Yeop Yu – *Center for Automotive Research, Department of Mechanical and Aerospace Engineering, The Ohio State University, Columbus, Ohio 43210, United States*

Adam Schmidt – *Center for Automotive Research, Department of Mechanical and Aerospace Engineering, The Ohio State University, Columbus, Ohio 43210, United States*

Cody O'Meara – *Center for Automotive Research, Department of Mechanical and Aerospace Engineering, The Ohio State University, Columbus, Ohio 43210, United States*

Jeremy Seidt – *Department of Mechanical and Aerospace Engineering, The Ohio State University, Columbus, Ohio 43210, United States*

Jay R. Sayre – *Department of Materials Science Engineering, The Ohio State University, Columbus, Ohio 43210, United States*

Yehia M. Khalifa – *Department of Chemistry and Biochemistry, The Ohio State University, Columbus, Ohio 43210, United States*

Complete contact information is available at: https://pubs.acs.org/10.1021/acsami.1c19554

Notes

The authors declare no competing financial interest.

■ ACKNOWLEDGMENTS

This work was supported in part by the United States Department of Energy under the "Cobalt-free Cathodes for Next Generation Li-Ion Batteries" project (contract no. DE-EE0008446) and by The Ohio State University Institute for Materials Research. Electron microscopy was performed at the Center for Electron Microscopy and Analysis (CEMAS) at The Ohio State University. The authors acknowledge the support of NSF-DMR (grant no. 0114098) for XPS instrument analysis performed at the Surface Analysis Lab (Dept. of Chemistry at The Ohio State University).

■ REFERENCES

(1) Tarascon, J.-M.; Armand, M. Issues and Challenges Facing Rechargeable Lithium Batteries. *Nature* **2001**, *414*, 359–367.

(2) Wood, D. L.; Li, J.; Daniel, C. Prospects for Reducing the Processing Cost of Lithium Ion Batteries. *J. Power Sources* **2015**, *275*, 234–242.

(3) Bigoni, F.; Giorgio, F. D.; Soavi, F.; Arbizzani, C. Sodium Alginate: A Water-Processable Binder in High-Voltage Cathode Formulations. *J. Electrochem. Soc.* **2017**, *164*, A6171−A6177.
(4) Patoux, S.; Daniel, L.; Bourbon, C.; Lignier, H.; Pagano, C.; Le Cras, F.; Jouanneau, S.; Martinet, S. High Voltage Spinel Oxides for Li-Ion Batteries: From the Material Research to the Application. *J. Power Sources* **2009**, *189*, 344−352.
(5) Kim, J.-H.; Myung, S.-T.; Sun, Y.-K. Molten Salt Synthesis of LiNi0.5Mn1.5O4 Spinel for 5 V Class Cathode Material of Li-Ion Secondary Battery. *Electrochim. Acta* **2004**, *49*, 219−227.
(6) Kraytsberg, A.; Ein-Eli, Y. Higher, Stronger, Better... A Review of 5 Volt Cathode Materials for Advanced Lithium-Ion Batteries. *Adv. Energy Mater.* **2012**, *2*, 922−939.
(7) Wentker, M.; Greenwood, M.; Leker, J. A Bottom-Up Approach to Lithium-Ion Battery Cost Modeling with a Focus on Cathode Active Materials. *Energies* **2019**, *12*, 504.
(8) Sun, Y.-K.; Lee, D.-J.; Lee, Y. J.; Chen, Z.; Myung, S.-T. Cobalt-Free Nickel Rich Layered Oxide Cathodes for Lithium-Ion Batteries. *ACS Appl. Mater. Interfaces* **2013**, *5*, 11434−11440.
(9) Kim, J.-H.; Pieczonka, N. P. W.; Li, Z.; Wu, Y.; Harris, S.; Powell, B. R. Understanding the Capacity Fading Mechanism in LiNi0.5Mn1.5O4/Graphite Li-Ion Batteries. *Electrochim. Acta* **2013**, *90*, 556−562.
(10) Kim, J.-H.; Pieczonka, N. P. W.; Yang, L. Challenges and Approaches for High-Voltage Spinel Lithium-Ion Batteries. *ChemPhysChem* **2014**, *15*, 1940−1954.
(11) Goodenough, J. B.; Kim, Y. Challenges for Rechargeable Li Batteries †. *Chem. Mater.* **2010**, *22*, 587−603.
(12) Pieczonka, N. P. W.; Borgel, V.; Ziv, B.; Leifer, N.; Dargel, V.; Aurbach, D.; Kim, J.-H.; Liu, Z.; Huang, X.; Krachkovskiy, S. A.; Goward, G. R.; Halalay, I.; Powell, B. R.; Manthiram, A. Lithium Polyacrylate (LiPAA) as an Advanced Binder and a Passivating Agent for High-Voltage Li-Ion Batteries. *Adv. Energy Mater.* **2015**, *5*, 1501008.
(13) Chong, J.; Zhang, J.; Xie, H.; Song, X.; Liu, G.; Battaglia, V.; Xun, S.; Wang, R. High Performance $LiNi_{0.5}Mn_{1.5}O_4$ Cathode Material with a Bi-Functional Coating for Lithium Ion Batteries. *RSC Adv.* **2016**, *6*, 19245−19251.
(14) Zheng, F.; Yang, C.; Xiong, X.; Xiong, J.; Hu, R.; Chen, Y.; Liu, M. Nanoscale Surface Modification of Lithium-Rich Layered-Oxide Composite Cathodes for Suppressing Voltage Fade. *Angew. Chem., Int. Ed.* **2015**, *54*, 13058−13062.
(15) Zhang, Z.; Zeng, T.; Lai, Y.; Jia, M.; Li, J. A Comparative Study of Different Binders and Their Effects on Electrochemical Properties of LiMn2O4 Cathode in Lithium Ion Batteries. *J. Power Sources* **2014**, *247*, 1−8.
(16) Guerfi, A.; Dontigny, M.; Charest, P.; Petitclerc, M.; Lagacé, M.; Vijh, A.; Zaghib, K. Improved Electrolytes for Li-Ion Batteries: Mixtures of Ionic Liquid and Organic Electrolyte with Enhanced Safety and Electrochemical Performance. *J. Power Sources* **2010**, *195*, 845−852.
(17) Lee, M.; Reddi, R. K. R.; Choi, J.; Liu, J.; Huang, X.; Cho, H.; Kim, J.-H. In-Operando AFM Characterization of Mechanical Property Evolution of Si Anode Binders in Liquid Electrolyte. *ACS Appl. Energy Mater.* **2020**, *3*, 1899−1907.
(18) Beaman, D. K.; Robertson, E. J.; Richmond, G. L. Unique Assembly of Charged Polymers at the Oil−Water Interface. *Langmuir* **2011**, *27*, 2104−2106.
(19) Grunlan, J. C.; Liu, L.; Kim, Y. S. Tunable Single-Walled Carbon Nanotube Microstructure in the Liquid and Solid States Using Poly(Acrylic Acid). *Nano Lett.* **2006**, *6*, 911−915.
(20) Li, J.; Le, D.-B.; Ferguson, P. P.; Dahn, J. R. Lithium Polyacrylate as a Binder for Tin−Cobalt−Carbon Negative Electrodes in Lithium-Ion Batteries. *Electrochim. Acta* **2010**, *55*, 2991−2995.
(21) Han, Z.; Zhan, H.; Zhou, Y. Preparation and Performance of Layered Li[Li 0.182 Ni 0.182 Co 0.091 Mn 0.545]O 2 Cathode with Different Binders. *Mater. Lett.* **2014**, *114*, 48−51.
(22) Kovalenko, I.; Zdyrko, B.; Magasinski, A.; Hertzberg, B.; Milicev, Z.; Burtovyy, R.; Luzinov, I.; Yushin, G. A Major Constituent of Brown Algae for Use in High-Capacity Li-Ion Batteries. *Science* **2011**, *334*, 75.
(23) Ingar Draget, K.; Østgaard, K.; Smidsrød, O. Homogeneous Alginate Gels: A Technical Approach. *Carbohydr. Polym.* **1990**, *14*, 159−178.
(24) Kuo, C. K.; Ma, P. X. Ionically Crosslinked Alginate Hydrogels as Sca!Olds for Tissue Engineering: Part 1. Structure, Gelation Rate and Mechanical Properties. 2001, 11.
(25) Liu, J.; Zhang, Q.; Wu, Z.-Y.; Wu, J.-H.; Li, J.-T.; Huang, L.; Sun, S.-G. A High-Performance Alginate Hydrogel Binder for the Si/C Anode of a Li-Ion Battery. *Chem. Commun.* **2014**, *50*, 6386.
(26) Sun, J.-Y.; Zhao, X.; Illeperuma, W. R. K.; Chaudhuri, O.; Oh, K. H.; Mooney, D. J.; Vlassak, J. J.; Suo, Z. Highly Stretchable and Tough Hydrogels. *Nature* **2012**, *489*, 133−136.
(27) Li, B.; Xing, L.; Xu, M.; Lin, H.; Li, W. New Solution to Instability of Spinel $LiNi_{0.5}Mn_{1.5}O_4$ as Cathode for Lithium Ion Battery at Elevated Temperature. *Electrochem. Commun.* **2013**, *34*, 48−51.
(28) Zhang, L.; Zhang, L.; Chai, L.; Xue, P.; Hao, W.; Zheng, H. A Coordinatively Cross-Linked Polymeric Network as a Functional Binder for High-Performance Silicon Submicro-Particle Anodes in Lithium-Ion Batteries. *J. Mater. Chem. A* **2014**, *2*, 19036−19045.
(29) Zhang, S.; Ren, S.; Han, D.; Xiao, M.; Wang, S.; Meng, Y. Aqueous Sodium Alginate as Binder: Dramatically Improving the Performance of Dilithium Terephthalate-Based Organic Lithium Ion Batteries. *J. Power Sources* **2019**, *438*, 227007.
(30) Gaikwad, A. M.; Arias, A. C. Understanding the Effects of Electrode Formulation on the Mechanical Strength of Composite Electrodes for Flexible Batteries. *ACS Appl. Mater. Interfaces* **2017**, *9*, 6390−6400.
(31) Song, J.; Jin, X.; Wang, X. C.; Jin, P. Preferential Binding Properties of Carboxyl and Hydroxyl Groups with Aluminium Salts for Humic Acid Removal. *Chemosphere* **2019**, *234*, 478−487.
(32) Preman, A. N.; Lee, H.; Yoo, J.; Kim, I. T.; Saito, T.; Ahn, S. Progress of 3D Network Binders in Silicon Anodes for Lithium Ion Batteries. *J. Mater. Chem. A* **2020**, *8*, 25548−25570.
(33) Jeena, M. T.; Lee, J.-I.; Kim, S. H.; Kim, C.; Kim, J.-Y.; Park, S.; Ryu, J.-H. Multifunctional Molecular Design as an Efficient Polymeric Binder for Silicon Anodes in Lithium-Ion Batteries. *ACS Appl. Mater. Interfaces* **2014**, *6*, 18001−18007.
(34) Kim, J.-H.; Pieczonka, N. P. W.; Lu, P.; Liu, Z.; Qiao, R.; Yang, W.; Tessema, M. M.; Sun, Y.-K.; Powell, B. R. In Situ Formation of a Cathode−Electrolyte Interface with Enhanced Stability by Titanium Substitution for High Voltage Spinel Lithium-Ion Batteries. *Adv. Mater. Interfaces* **2015**, *2*, 1500109.
(35) Pieczonka, N. P. W.; Liu, Z.; Lu, P.; Olson, K. L.; Moote, J.; Powell, B. R.; Kim, J.-H. Understanding Transition-Metal Dissolution Behavior in LiNi0. 5Mn1. 5O4 High-Voltage Spinel for Lithium Ion Batteries. *J. Phys. Chem. C* **2013**, *117*, 15947−15957.
(36) Schmidt, J. P.; Chrobak, T.; Ender, M.; Illig, J.; Klotz, D.; Ivers-Tiffée, E. Studies on LiFePO4 as Cathode Material Using Impedance Spectroscopy. *J. Power Sources* **2011**, *196*, 5342−5348.
(37) Hu, L.; Xue, Z.; Amine, K.; Zhang, Z. Fluorinated Electrolytes for 5-V Li-Ion Chemistry: Synthesis and Evaluation of an Additive for High-Voltage $LiNi_{0.5}Mn_{1.5}O_4$ /Graphite Cell. *J. Electrochem. Soc.* **2014**, *161*, A1777−A1781.
(38) Pieczonka, N. P. W.; Yang, L.; Balogh, M. P.; Powell, B. R.; Chemelewski, K.; Manthiram, A.; Krachkovskiy, S. A.; Goward, G. R.; Liu, M.; Kim, J.-H. Impact of Lithium Bis(Oxalate)Borate Electrolyte Additive on the Performance of High-Voltage Spinel/Graphite Li-Ion Batteries. *J. Phys. Chem. C* **2013**, *117*, 22603−22612.
(39) Yang, L.; Ravdel, B.; Lucht, B. L. Electrolyte Reactions with the Surface of High Voltage LiNi0.5Mn1.5O4 Cathodes for Lithium-Ion Batteries. *Electrochem. Solid-State Lett.* **2010**, *13*, A95−A97.
(40) Lu, L.; Han, X.; Li, J.; Hua, J.; Ouyang, M. A Review on the Key Issues for Lithium-Ion Battery Management in Electric Vehicles. *J. Power Sources* **2013**, *226*, 272−288.

https://doi.org/10.1021/acsami.1c19554
ACS Appl. Mater. Interfaces 2022, 14, 861−872

(41) Zhong, H.; He, J.; Zhang, L. Better Cycle Stability and Rate Capability of High-Voltage LiNi 0.5 Mn 1.5 O 4 Cathode Using Water Soluble Binder. *Mater. Res. Bull.* **2017**, *93*, 194−200.
(42) Dong, T.; Zhang, H.; Ma, Y.; Zhang, J.; Du, X.; Lu, C.; Shangguan, X.; Li, J.; Zhang, M.; Yang, J.; Zhou, X.; Cui, G. A Well-Designed Water-Soluble Binder Enlightening the 5 V-Class LiNi0.5Mn1.5O4 Cathodes. *J. Mater. Chem. A* **2019**, 8.
(43) Aurbach, D.; Markovsky, B.; Weissman, I.; Levi, E.; Ein-Eli, Y. On the Correlation between Surface Chemistry and Performance of Graphite Negative Electrodes for Li Ion Batteries. *Electrochim. Acta* **1999**, *45*, 67−86.
(44) Ma, Y.; Chen, K.; Ma, J.; Xu, G.; Dong, S.; Chen, B.; Li, J.; Chen, Z.; Zhou, X.; Cui, G. A Biomass Based Free Radical Scavenger Binder Endowing a Compatible Cathode Interface for 5 V Lithium-Ion Batteries. *Environ. Sci.* **2019**, 8.
(45) Hekmatfar, M.; Kazzazi, A.; Eshetu, G. G.; Hasa, I.; Passerini, S. Understanding the Electrode/Electrolyte Interface Layer on the Li-Rich Nickel Manganese Cobalt Layered Oxide Cathode by XPS. *ACS Appl. Mater. Interfaces* **2019**, *11*, 43166−43179.
(46) Dong, T.; Mu, P.; Zhang, S.; Zhang, H.; Liu, W.; Cui, G. How Do Polymer Binders Assist Transition Metal Oxide Cathodes to Address the Challenge of High-Voltage Lithium Battery Applications? *Electrochem. Energy Rev.* **2021**, *4*, 545−565.
(47) Nguyen, C. C.; Lucht, B. L. Comparative Study of Fluoroethylene Carbonate and Vinylene Carbonate for Silicon Anodes in Lithium Ion Batteries. *J. Electrochem. Soc.* **2014**, *161*, A1933−A1938.
(48) Lu, M.; Cheng, H.; Yang, Y. A Comparison of Solid Electrolyte Interphase (SEI) on the Artificial Graphite Anode of the Aged and Cycled Commercial Lithium Ion Cells. *Electrochim. Acta* **2008**, *53*, 3539−3546.
(49) Pan, J.; Cheng, Y.-T.; Qi, Y. General Method to Predict Voltage-Dependent Ionic Conduction in a Solid Electrolyte Coating on Electrodes. *Phys. Rev. B* **2015**, *91*, 134116.

https://doi.org/10.1021/acsami.1c19554
ACS Appl. Mater. Interfaces 2022, 14, 861−872